Cancer Research

Assessing Prostate Cancer Aggressiveness with Hyperpolarized Dual-Agent 3D Dynamic Imaging of Metabolism and Perfusion

Hsin-Yu Chen[1,2,3], Peder E.Z. Larson[1,2,3], Robert A. Bok[3], Cornelius von Morze[3], Renuka Sriram[3], Romelyn Delos Santos[3], Justin Delos Santos[3], Jeremy W. Gordon[3], Naeim Bahrami[3,4], Marcus Ferrone[5], John Kurhanewicz[1,2,3], and Daniel B. Vigneron[1,2,3]

Abstract

New magnetic resonance (MR) molecular imaging techniques offer the potential for noninvasive, simultaneous quantification of metabolic and perfusion parameters in tumors. This study applied a three-dimensional dynamic dual-agent hyperpolarized ^{13}C magnetic resonance spectroscopic imaging approach with ^{13}C-pyruvate and ^{13}C-urea to investigate differences in perfusion and metabolism between low- and high-grade tumors in the transgenic adenocarcinoma of mouse prostate (TRAMP) transgenic mouse model of prostate cancer. Dynamic MR data were corrected for T1 relaxation and RF excitation and modeled to provide quantitative measures of pyruvate to lactate flux (k_{PL}) and urea perfusion (urea AUC) that correlated with TRAMP tumor histologic grade. k_{PL} values were relatively higher for high-grade TRAMP tumors. The increase in k_{PL} flux correlated significantly with higher lactate dehydrogenase activity and mRNA expression of *Ldha*, *Mct1*, and *Mct4* as well as with more proliferative disease. There was a significant reduction in perfusion in high-grade tumors that associated with increased hypoxia and mRNA expression of *Hif1α* and *Vegf* and increased k_{trans}, attributed to increased blood vessel permeability. In 90% of the high-grade TRAMP tumors, a mismatch in perfusion and metabolism measurements was observed, with low perfusion being associated with increased k_{PL}. This perfusion-metabolism mismatch was also associated with metastasis. The molecular imaging approach we developed could be translated to investigate these imaging biomarkers for their diagnostic and prognostic power in future prostate cancer clinical trials. *Cancer Res; 77(12); 3207–16. ©2017 AACR.*

Introduction

A pressing need facing the clinical management of prostate cancer patients is an accurate method for distinguishing aggressive, potentially lethal prostate cancer from indolent disease. Prostate cancer is the second most prevalent cancer in American men, with 1 in 6 being diagnosed, but is fatal in only 12% of these cases (1). Active surveillance has emerged as an appropriate management technique for patients in whom disease is likely to be indolent (tumors $\leq$ 0.5 cc and Gleason grade $\leq$ 3+3; ref. 2). New focal therapy approaches are also being considered for men with defined regions of localized intermediate risk prostate cancer (moderate size cancers with secondary Gleason 4 pattern) that can be clearly identified on imaging (3, 4), whereas patients with more aggressive but localized disease are treated with surgical or radiotherapy. Therefore, the ability to localize and provide a noninvasive imaging assessment of cancer aggressiveness has become critically important for clinical management of men with prostate cancer. The current state-of-the-art for imaging localized prostate cancer, multiparametric ^{1}H MRI, has demonstrated the ability to localize tumors for subsequent biopsy and treatment, but cannot consistently grade tumor aggressiveness accurately in individual patients (4).

Increasing evidence points to prostate cancer being a disease strongly linked to abnormal metabolism due to changes in key metabolic enzymes (5). Also, tumor microenvironment factors such as perfusion (6) have been associated with the presence and aggressiveness of prostate cancer. In this study, a new dual-agent hyperpolarized (HP) ^{13}C MRI approach was investigated to characterize aggressive cancers based on their metabolic and perfusion abnormalities and applied to a preclinical mouse model of prostate cancer. The development and progression of prostate cancer in the transgenic adenocarcinoma of mouse prostate (TRAMP) model mimics many aspects of human prostate cancer (7). Specifically, cancer development in the TRAMP model is targeted to the prostate and tumors progress from primary androgen dependent to large androgen-independent tumors with metastases. In addition, most male TRAMP mice develop tumors that are pathologically similar to human prostate cancer and are large enough for MRI studies (8). Metabolically, the TRAMP model has demonstrated changes in TCA metabolism and glycolysis associated with the evolution and progression of prostate cancer in patients (7).

Hyperpolarized ^{13}C MRI is a powerful new metabolic imaging method that uses specialized instrumentation to provide signal

[1]Graduate Program in Bioengineering, University of California, San Francisco, San Francisco, California. [2]Graduate Program in Bioengineering, University of California, Berkeley, Berkeley California. [3]Department of Radiology and Biomedical Imaging, University of California, San Francisco, San Francisco, California. [4]Masters of Science in Biomedical Imaging Program, University of California, San Francisco, San Francisco, California. [5]Department of Clinical Pharmacy, University of California, San Francisco, San Francisco, California.

Note: Supplementary data for this article are available at Cancer Research Online (http://cancerres.aacrjournals.org/).

Corresponding Author: Daniel B. Vigneron, University of California, San Francisco, 1700 4th Street, Byers Hall Suite 102, MC 2512, San Francisco, CA 94158-2330. Phone: 415-476-3343; Fax: 415-514-4451; E-mail: Dan.Vigneron@ucsf.edu

doi: 10.1158/0008-5472.CAN-16-2083

enhancements of over 10,000-fold for ^{13}C enriched, safe, endogenous, nonradioactive compounds (9). Although prostate cancer is often inadequately evaluated using FDG-PET (which assesses glucose uptake and phosphorylation; refs. 10, 11), HP ^{13}C MR detects downstream metabolism, specifically the metabolic flux of HP ^{13}C-pyruvate to lactate (k_{PL}) catalyzed by lactate dehydrogenase (LDH). This method has shown great potential for not only detecting prostate cancer, but for also assessing the aggressiveness (pathologic grade) of the cancer (12). The "Warburg effect," an elevation in glycolysis and lactate production in the presence of oxygen, occurs in prostate cancer and is due to multiple factors, including oncogenic modulations, mitochondrial dysfunction, as well as an adaptive response to the tumor microenvironment to promote proliferation (13). A prior single time-point ^{13}C magnetic resonance spectroscopic imaging (MRSI) study of hyperpolarized ^{13}C-pyruvate metabolism in the TRAMP model demonstrated a significant increase in hyperpolarized ^{13}C-lactate in high- versus low-grade prostate tumors (12). The unprecedented gain in sensitivity provided by hyperpolarization can be combined with fast spectroscopic ^{13}C MRSI techniques to provide spatially resolved dynamic data of hyperpolarized pyruvate metabolism (14). These dynamic data can be fit to kinetic models (15) to obtain the flux of HP ^{13}C-pyruvate to lactate catalyzed by LDH rather than a single time-point measurement of hyperpolarized ^{13}C-lactate, which is very sensitive to differences in the timing of probe delivery, and when the imaging data are acquired. Another important feature of HP ^{13}C MRSI is that it encodes chemical as well as spatial information, thereby providing the potential for using multiple hyperpolarized ^{13}C-labeled agents to detect several metabolic and/or physiologic processes simultaneously after the injection of a single bolus (16). HP ^{13}C-urea is not taken up and metabolized by most tissues, and prior publications have demonstrated that hyperpolarized ^{13}C-urea provides a reproducible and accurate assessment of blood perfusion in animal cancer models (16, 17). Methods for copolarizing ^{13}C-pyruvate and ^{13}C-urea have been developed, successfully polarized, and injected in preclinical models to simultaneously measure perfusion and metabolism (16).

The goal of this study was to use a three-dimensional (3D) dynamic, dual-agent, ^{13}C-pyruvate and ^{13}C-urea, HP ^{13}C MRSI approach to investigate differences in perfusion and metabolism metrics between high- and low-grade tumors in the TRAMP model.

Materials and Methods

Animal protocol and handling

All animal studies were conducted in accordance with the policies of Institutional Animal Care and Use Committee at University of California, San Francisco. The TRAMP model, supplied by Roswell Park Cancer Institute, was generated in a C57BL/6 background utilizing a transgene consisting of a 7426/28 bp fragment of the rat *probasin* (*rPB*) gene directing the tissue-specific expression of simian virus 40 (SV40) early genes (T/t antigens; Tag) to the mouse prostate epithelium to abrogate the activity of the p53 and Rb tumor suppressors (8). The 19 TRAMP mice utilized in this study were cannulated using a 32-gauge IV catheter in the lateral tail vein and anesthetized with 1% to 1.5% isoflurane/100% oxygen at a rate of 1 L/min on a heated water bed to maintain physiological body temperature.

MR imaging

The imaging studies were performed on a 3T MR scanner (MR750, GE Healthcare) using a custom-built dual-tuned ^{13}C-proton quadrature murine coil. Dynamic HP ^{13}C spectral data were acquired after a tail vein injection of 350 μL of copolarized 80 mmol/L [1-^{13}C]pyruvate and ^{13}C urea (details in Supplementary Materials and Methods) using a 3D HP ^{13}C compressed sensing (CS) EPSI sequence (14) with a field of view (FOV) of 4 cm x 4 cm x 8.6 cm, a spectral BW of 581 Hz, with a spatial resolution of 3.3 mm x 3.3 mm x 5.4 mm, and a temporal resolution of 2 seconds. Eighteen time-points were acquired starting immediately after the 15-second injection. Anatomic reference images were acquired using a T_2-weighted Fast Spin Echo (FSE) sequence (spatial resolution: 0.23 mm, FOV: 6 cm, TE/TR = 102/5,821 ms).

Histopathologic analysis

TRAMP mice were euthanized and dissected within 6 hours after the MRI study. To measure tumor hypoxia, Pimonidazole (PIM) solution was injected approximately 45 minutes prior to euthanization. Dissection was performed by an experienced uro-oncologist, and digital images were taken as a reference for localization and registration of tumor specimens. The excised tissue was aliquoted for histochemical processing, gene expression, and activity analyses (details in Supplementary Materials and Methods). The histologic index, as defined in Albers and colleagues, was used to pathologically define high- versus low-grade TRAMP tumors in this study (12). A histologic index was calculated based on the weighted percentages of tumor differentiation (normal, well-differentiated, moderately well differentiated, and poorly differentiated) from standard hematoxylin and eosin (H&E) staining. The histologic index ranged between 0 and 3, where 0 indicated that 100% of the tissue was normal and 3 indicated that 100% of the tissue was poorly differentiated. In the Albers' publication as in this one, the tumors were dichotomized to be either low grade (index ≤ 1) or high grade (index ≥ 2) in a manner that reflects the clinical pathologic situation in which patients with Gleason score $\leq 3+3$ are considered to have low versus Gleason $\geq 3 + 4$ high-grade tumors. In all cases, the histologic assessments were determined from what were considered globally representative sections of the tumor masses.

Metastases were detected and enumerated at the time of primary tumor dissection, by careful, systematic, visual inspection, and concomitant photography of the abdominal and thoracic cavity contents, starting in the pelvic area with identification/inspection of pelvic and para-aortic lymph nodes, then moving to the mid-abdomen with inspection of the kidneys, perirenal lymph nodes, and mesentery, then moving to the upper abdomen, removing the liver and inspecting the surfaces of all its lobes, and lastly inspecting the thoracic cavity, particularly the lungs for any parenchymal metastases and the mediastinum area for any adenopathy. All visually identified metastatic lesions were confirmed by subsequent histologic examination.

Data processing

The HP MRSI data were reconstructed using a CS approach (details in Supplementary Materials and Methods; ref. 18). As shown in Fig 1, this processing resulted in 3D arrays (Fig. 1A) of dynamic HP ^{13}C spectra (Fig. 1B), demonstrating resonances due to ^{13}C-urea, [1-^{13}C]alanine, [1-^{13}C]pyruvate, and [1-^{13}C]lactate.

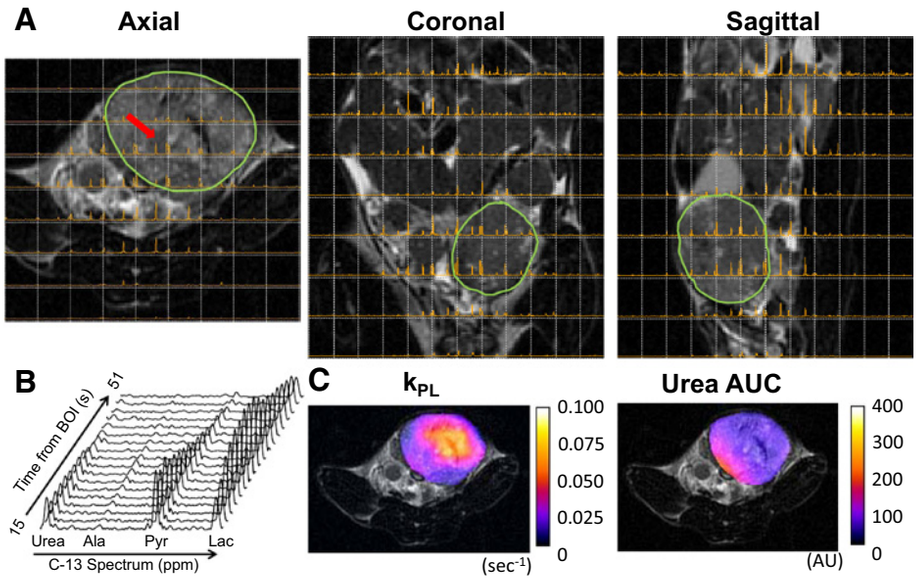

Figure 1.
A, *In vivo* 3D ^{13}C MR spectral arrays shown at a single time point taken 20 seconds after injection of copolarized HP ^{13}C-pyruvate in the axial, coronal, and sagittal planes overlaid on T_2-weighted anatomic references. The spectra have an anterior–posterior and right–left resolution of 3.3 mm and a superior–inferior resolution of 5.4 mm. The primary tumor is outlined in green. **B,** Dynamic data (2s temporal resolution) shown for a representative 0.059 cm^3 voxel in the center of the TRAMP tumor (red arrow) demonstrating resonances of ^{13}C-urea, [1-^{13}C]pyruvate, and the metabolic products [1-^{13}C]lactate, [1-13C]alanine. **C,** Corresponding axial pyruvate-to-lactate conversion rate k_{PL} and urea AUC images overlaid on T_2-FSE anatomic references, respectively.

Coregistration of the histologic sections and HP ^{13}C MRI data was achieved by cutting multiple sections of tumors in the same axial plane as the MRI images and taking care to mark various surfaces of primary tumors *in situ* with surgical dyes. Where possible, anatomic landmarks, such as urethra and bladder, were also utilized to help register histologic cross-sections with the MRI sections. Although data were zero filled for display purposes, quantitation of the HP ^{13}C MR data was performed using the native acquisition resolution of the data. The ROIs incorporating the tumor were defined using the anatomic T_2w images as reference, and only voxels that were > 85% in the tumor were quantified. Necrotic regions could be also visualized on the T_2w images, and these voxels were found to have low S/N, so the spectral S/N filter (SNR < 4) employed removed necrotic voxels from the analysis. All preprocessing of ^{13}C data, including reorganizing the k-space and l_1-minimization and signal filtering, were performed using MATLAB (Mathworks), and the data were displayed using the open-source SIVIC package (19).

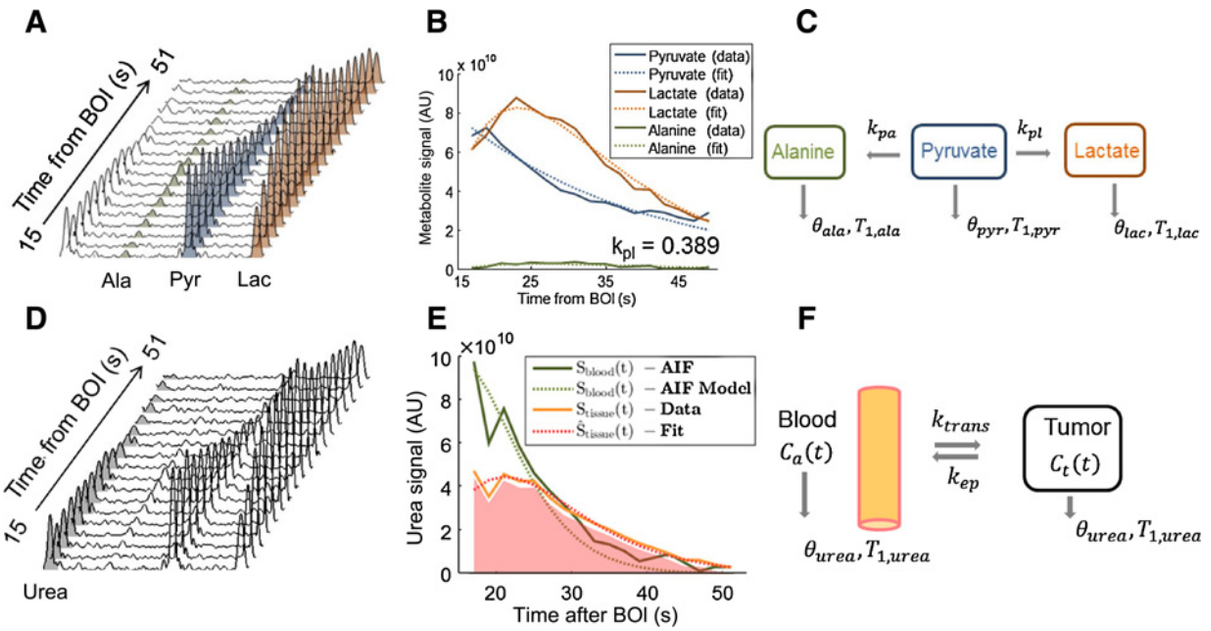

Figure 2.
A, Dynamic hyperpolarized spectral data acquired after injection of HP [1-^{13}C]pyruvate. **B** and **C,** Plot showing the raw signal intensities of pyruvate, lactate, alanine versus time (solid line), and the corresponding modeled metabolic data (dash line) used to determine k_{PL} (**B**) as shown in the flow diagram (**C**) and described in Materials and Methods. **D,** HP ^{13}C urea signals were extracted from the tumor and from nearby vessels to define an AIF. **E,** Fitting dynamic models to urea signal curves, with shaded region showing urea AUC. **F,** Two-compartment model for calculating the rate constant k_{trans}. AU, arbitrary units.

Modeling of k_{PL} and k_{trans}

HP [1-^{13}C]pyruvate to [1-^{13}C]lactate flux (k_{PL}) was modeled using a two-compartment model as shown in Fig. 2C, described in the following equations:

$$\frac{dM_{lac}(t)}{dt} = k_{PL}M_{pyr}(t) - \left(1/T_{1,lac}\right)M_{lac} \quad \text{(A)}$$

$$\frac{dM_{pyr}(t)}{dt} = -(k_{PL} + k_{PA})M_{pyr}(t) - \left(1/T_{1,pyr}\right)M_{pyr}(t) \quad \text{(B)}$$

$$M_x{}^{+}[n] = M_x{}^{-}[n] \cdot \cos\theta_n \quad \text{(C)}$$

$$S_x[n] = M_x{}^{-}[n] \cdot \sin\theta_n \quad \text{(D)}$$

where $M_x(t)$ is the longitudinal magnetization of metabolite x, k_{PL} is the pyruvate-to-lactate flux, k_{PA} is the pyruvate-to-alanine flux (Alanine was included in modeling), and $T_{1,x}$ is the spin-lattice relaxation time. $M_x{}^{+}[n]$ and $M_x{}^{-}[n]$ represent the net HP ^{13}C magnetization before and after the n^{th} RF excitation (with flip angle θ_n), and $S_x[n]$ is the observed metabolite signal.

Quantitatively, perfusion, and permeability can be reflected by the dynamic bio-distribution of HP ^{13}C-urea between blood and tissue *in vivo* similar to the above equation (Fig. 2F).

$$\frac{dC_{tissue}(t)}{dt} = k_{trans}C_{blood}(t) - k_2C_{tissue}(t) \quad \text{(E)}$$

where $C_{blood}(t)$ represents the arterial input function (AIF), $C_{tissue}(t)$ is the time-resolved concentration in tissue, and k_{trans} (20) and k_2 are modified forward and reverse perfusion coefficients, respectively. In the nonlinear numerical fitting, the reverse perfusion coefficient k_{ep} and the relaxation T_1 are highly linearly-dependent variables. Therefore, we combined k_{ep} and T_1 into a generalized term k_2. The coefficient k_2 reflects the combined effect of physiology and longitudinal relaxation. The summed HP ^{13}C-urea peak area under dynamic curve (AUC) was also calculated and normalized to kidney urea AUC. Normalized urea AUC provides a measure of the tracer distribution in tissue, whereas k_{trans} provides combined measure of perfusion and permeability (20). For the AUC metric, although a rigorous definition of timing requires an offset t_0 in the parameter models, the definition used should be reasonable given the relatively consistent urea peak position (±3 seconds) observed (Fig. 7).

Numerical fitting of the *in-vivo* dynamic data to the two-compartment model was performed using nonlinear least squares algorithm for both dynamic HP [1-^{13}C]pyruvate (Fig. 2B) and HP ^{13}C-urea signals (Fig. 2E). The multiband variable flip excitation scheme (θ) and spin lattice (T_1) relaxation times were taken into account as sources of signal loss using a hybrid continuous-discrete time dynamical system (15). The reverse flux of HP [1-^{13}C]lactate to HP [1-^{13}C]pyruvate was excluded from the models because it has been determined to be negligible in TRAMP tumors (21), and a lower number of free variables improves fitting stabilization. The MATLAB-based fitting iterates until a local minimum in object function is arrived from the initial values.

Statistical analyses

Average values of k_{PL}, urea AUC, and urea k_{trans} were calculated from the entire TRAMP tumor, excluding regions of necrosis, using the T_2-weighted anatomic reference image to identify the tumor. Ki-67 and PIM immunohistochemical staining were reported as the mean fraction of cells (average ± stdev) staining positive. mRNA expression data are reported as relative changes to housekeeping genes. Significance was reported using the standard Mann–Whitney–Wilcoxon test comparing all measured parameters in low- versus high-grade TRAMP tumors (MATLAB) and at 3 significance levels, i.e., P values of <0.05, $P < 0.01$, $P < 0.001$.

Results

Hyperpolarized ^{13}C dynamic MRSI data were acquired on a total of 19 TRAMP mice, 10 with high- and 9 with low-grade tumors. The FOV of the dynamic CS-EPSI sequence (FOV—4 × 4 × 8.6 cm) enabled three-dimensional detection of hyperpolarized ^{13}C spectra throughout the primary tumor and from the majority of mouse abdomen. Figure 1A shows representative HP ^{13}C MR spectra in the axial, coronal, and sagittal planes acquired 21 seconds after the injection of HP [1-^{13}C]pyruvate. Figures 1B, 2A, and 2D show representative dynamic HP ^{13}C spectra (2-second temporal resolution) taken from a single voxel from the center of the TRAMP tumor shown in Fig. 1A (red arrow). The dynamic HP ^{13}C spectral acquisition started at approximately 15 seconds from the start of injection of the hyperpolarized solution, at which time the HP [1-^{13}C]pyruvate signal was near maximum (t ≈ 15–20 seconds). Also at this time-point, the metabolic products, HP [1-^{13}C]lactate and [1-^{13}C]alanine, were already observed in the TRAMP tumor and reached maximum signal

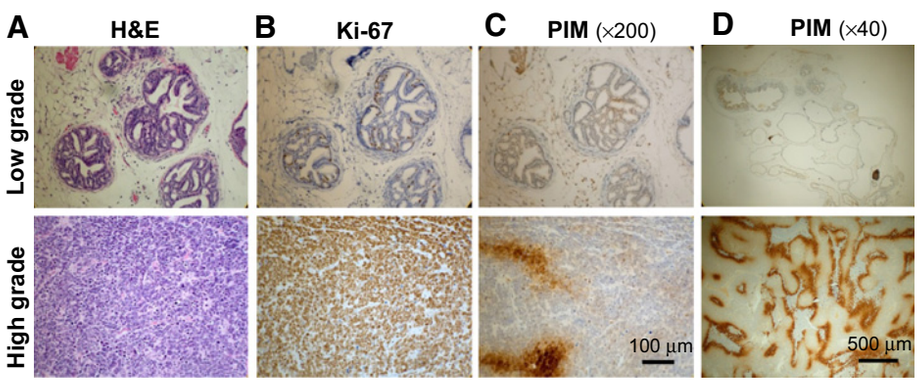

Figure 3.
Immunochemical staining of excised representative low- and high-grade TRAMP tumors; H&E section (**A**), Ki-67 staining (**B**), and PIM staining (**C**). The micrographs in **A–C** were taken under ×200 magnification and PIM staining (**D**) under ×40 magnification.

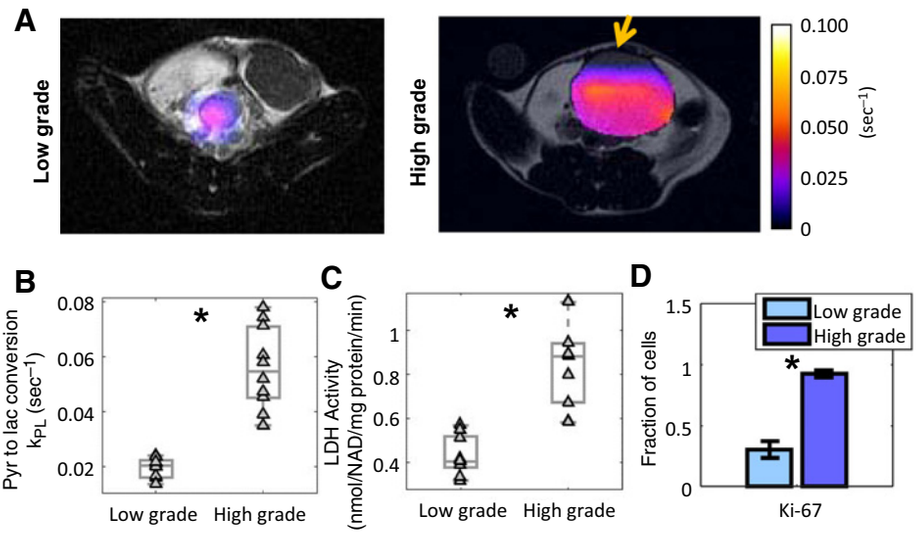

Figure 4.

A, Representative calculated pyruvate-to-lactate flux (k_{PL}) images overlaid on corresponding T_2-FSE reference images from a low-grade (left) and a high-grade (right) TRAMP tumor. At pathology, a region of necrosis was observed in the anterior aspect of the tumor (red arrow). **B,** Box plots showing individual (diamonds), median, and standard deviation k_{PL} flux measurements in the 9 low-grade and 10 high-grade TRAMP tumors. **C,** A bar plot showing the fraction of cells staining positive for Ki-67 (mean ± SE). **D,** LDH activities for the same TRAMP tumors. *, significantly different; $P < 0.001$.

intensity at approximately 25 to 30 seconds and 30 to 35 seconds, respectively. Similar to HP [1-^{13}C]pyruvate, HP-^{13}C urea had a maximal signal intensity at approximately 15 to 20 seconds. The timing of the dynamic data acquired for HP [1-^{13}C]pyruvate, [1-^{13}C]lactate, [1-^{13}C]alanine, and ^{13}C-urea was not different between low- and high-grade tumors.

Figure 2 depicts the analysis of the dynamic spectral data including correction for T_1 relaxation and flip-angle and modeling to provide quantitative measures of pyruvate-to-lactate rate constants (k_{PL}) and k_{trans}. Representative fits of the dynamic HP [1-^{13}C]pyruvate and HP ^{13}C-urea data to obtain k_{PL} and k_{trans} are shown in Fig. 2B and E. Spatially interpolated maps of k_{PL} and urea AUC were overlaid on the corresponding anatomic reference image (Fig. 1C). The k_{PL} and urea overlays were restricted to the region of the tumor as identified on the T_2-weighted anatomic reference image. In Fig. 1C, the mismatch between urea AUC and metabolism is clearly seen in comparing the k_{PL} and urea AUC images of the high-grade tumor. Areas of this TRAMP tumor that demonstrated the lowest urea AUC (≈75–100 units) also showed the highest k_{PL} (0.055–0.075 sec^{-1}). This mismatch between metabolism and urea AUC was observed in 9 of 10 of the high-grade TRAMP tumors studied, and this mismatch was not observed in any of the low-grade tumors. In addition, 50% of the high-grade tumors demonstrated either lymph node or liver metastases, with mice having low-grade tumors not demonstrating any metastases.

Representative immunochemical-stained tissue sections from low- and high-grade TRAMP tumors are shown in Fig. 3. Similar to the human prostate, normal murine prostate histology is highly glandular with secretory epithelial cells lining glands and stromal tissue supporting the glands (not shown). The H&E histologic sections from the low- and high-grade tumors (Fig. 3A) depict the gradual replacement of the secretory epithelial cells by less differentiated epithelial cells until the glands were completely eliminated and only sheets of pleomorphic cells with irregular nuclei remained in the high-grade tumors. High-grade TRAMP tumors also demonstrated higher Ki-67 (Fig. 3B) and PIM (Fig. 3C) staining as compared with low-grade TRAMP tumors.

Pyruvate to lactate flux images overlaid on corresponding T_2-FSE anatomic reference images from a representative low- and a high-grade TRAMP tumor (Fig. 4A) demonstrated a heterogeneous but higher k_{PL} flux in the high-grade tumor. Also in this high-grade tumor, there was a region of necrosis observed at pathology in the anterior aspect of the tumor associated with undetectable k_{PL} (red arrow). Pyruvate to lactate flux (k_{PL}) values (Fig. 4B) were significantly ($P < 0.001$) higher (0.056 ± 0.005 sec^{-1} vs. 0.019 ± 0.001 sec^{-1}) for high- versus low-grade TRAMP tumors with no overlap of individual k_{PL} values between the 2 groups in this study. The increase in k_{PL} flux significantly correlated with higher LDH activity (0.85 ± 0.06 vs. low-grade: 0.43 ± 0.03, mmol/L/mg protein/min, $P < 0.001$) in high- versus low-grade tumors (Fig. 4D). Also, the high-grade TRAMP tumors were found to be more proliferative with a significantly ($P < 0.001$) larger portion of the tumor staining positive for Ki-67 than for low-grade tumors (95 ± 3% vs. 30 ± 7%). The alanine conversion was 1 to 2 orders of magnitude smaller than k_{PL}, and there was no difference between high- and low- grade tumors (k_{PA} low-grade: 0.002 ± 0.001 sec^{-1}, high-grade: 0.004 ± 0.001 sec^{-1}, $P > 0.4$).

Figure 5A shows urea AUC images overlaid on reference anatomic images of the same animals shown in Fig. 4A, visually demonstrating heterogeneous but higher urea AUC in the low- versus high-grade tumor. A quantitative comparison of urea AUC and k_{trans} for the low- and high-grade tumors is shown in Fig. 5B. Urea AUC was significantly reduced ($P < 0.01$, 640 ± 94 as compared with the 1,407 ± 221 AU), whereas k_{trans} significantly increased ($P < 0.01$, 358 ± 38 as compared with 180 ± 24 mL/dL/min) in high- versus low- grade tumors. The hypoxia was also significantly ($P < 0.05$) increased in high- relative to low-grade prostate cancer (27 ± 6% vs. 14 ± 4% of the tumor staining positive for PIM, respectively), as measured by PIM immunohistochemical staining (Fig. 5D). Interestingly, no significant difference was found in microvessel density between high- and low-grade TRAMP tumors (high-grade = 14.3 ± 1.7, low-grade = 14.7 ± 2.1 vessels/hpf 200x, $P > 0.5$).

Figure 6 summarizes the expression of key transporters and enzymes associated with pyruvate transport and metabolism (*Mct1* and *Mct4*, *Ldha*, and *Ldhb*) and of factors affected by the hypoxic tumor microenvironment (*Hif1α* and *Vegf*). Expression of the monocarboxylate transporters *Mct1* and *Mct4* was significantly upregulated (*Mct1*: 2.75 ± 0.72-fold, $P < 0.05$, *Mct4*: 20.7 ± 7.12-fold, $P < 0.01$) in high- versus low-grade TRAMP tumors. *Ldha* was significantly increased 1.98 ± 0.22-fold

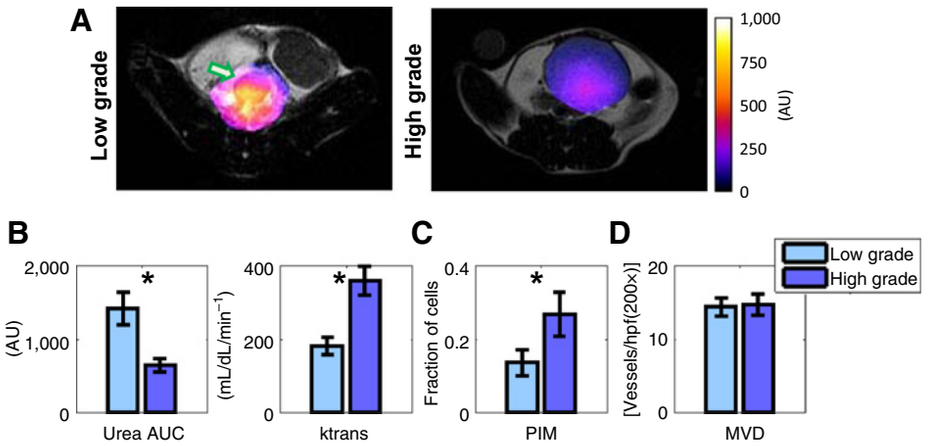

Figure 5.
A, Representative calculated urea AUC images overlaid on the corresponding T_2-FSE anatomic reference images from a low-grade (right) and a high-grade TRAMP tumor. **B,** Bar plots showing average ± SE for urea AUC and k_{trans}. $P < 0.01$. AU, arbitrary units. **C,** Fraction of cells staining positive for PIM in the 9 low-grade and 10 high-grade TRAMP tumors studied. $P < 0.05$. **D,** No difference found in representative microvascular density (MVD) assessed by CD31 IHC staining (3 high-grade vs. 3 low-grade). *, significantly different.

($P < 0.01$) and *Ldhb* significantly decreased to 0.13 ± 0.05- fold ($P < 0.01$), leading to a dramatic 15.0 ± 4.8-fold increase ($P < 0.001$) in the *Ldha*/*Ldhb* ratio in high- versus low-grade TRAMP tumors. Due to increased hypoxia in the tumor microenvironment (higher PIM staining), there was a significant 3.64 ± 0.55-fold ($P < 0.01$) and 6.40 ± 1.82-fold ($P < 0.01$) increase in *Hif1α* and *Vegf* expression, respectively, in high- versus low-grade TRAMP tumors.

Discussion and Conclusions

An accurate assessment of the aggressiveness of prostate cancer requires the complete coverage of the prostate at high spatial resolution due to the often small, multifocal, and biologically diverse nature of this disease. In this study, a volumetric dynamic dual-agent hyperpolarized ^{13}C spectroscopic imaging approach using ^{13}C-pyruvate and ^{13}C-urea to simultaneously image changes in urea AUC and pyruvate metabolism with prostate cancer progression was performed for the first time in a transgenic murine model of prostate cancer. The 20,000- to 40,000-fold enhancement in signal-to-noise relative to the respective thermal MR signals at 3T provided by the copolarization of ^{13}C-pyruvate and ^{13}C-urea combined with fast volumetric ^{13}C spectroscopic imaging allowed for both high spatial (0.06 cm^3) and temporal (2 seconds) resolution imaging data to be acquired throughout the primary prostate tumor and the body of the mouse. This dynamic metabolic and perfusion data were fit to kinetic models (15) to obtain the flux of HP ^{13}C-pyruvate to lactate (k_{PL}) catalyzed by LDH and k_{trans}, a measure of both perfusion and vascular permeability. In addition, an estimate of tumor urea tissue distribution was calculated using the area under curve of hyperpolarized ^{13}C-urea signal (16, 17). Moreover, the ability to dynamically measure urea delivery, tissue distribution, and pyruvate metabolism allows for differences in the timing of hyperpolarized probe delivery and metabolism that can occur between individual subjects. Although these differences in dynamics were small (2–5 seconds), they can add substantially to the variability of single time-point hyperpolarized ^{13}C-lactate to ^{13}C-pyruvate ratio measurements, because the ^{13}C-pyruvate signal is dramatically decreasing due to T_1 relaxation and metabolism during the spectral acquisition (12).

There is growing evidence that the upregulation of aerobic glycolysis and increased lactate production and efflux is an adaptation of cancer cells that aids in survival, growth, and metastasis and often leads to poor response to therapy (22, 23). The results of this study indicate that increased hyperpolarized ^{13}C-pyruvate to lactate flux (k_{PL}) is associated with more aggressive prostate cancer. Specifically, the k_{PL} was 3-fold higher in high- relative to low-pathologic grade prostate tumors, with no overlap between k_{PL} values from individual high- and low-grade tumors. High-grade TRAMP tumors were also more proliferative, having 3-fold higher Ki-67 staining than low-grade tumors. In concordance with the HP ^{13}C-pyruvate-to-lactate metabolism data, there was a 2-fold increase in tissue LDH activity, as measured *ex vivo*, in the same high- relative to low-grade tumors. Because the measurement of HP lactate signal generation is in non–steady-state

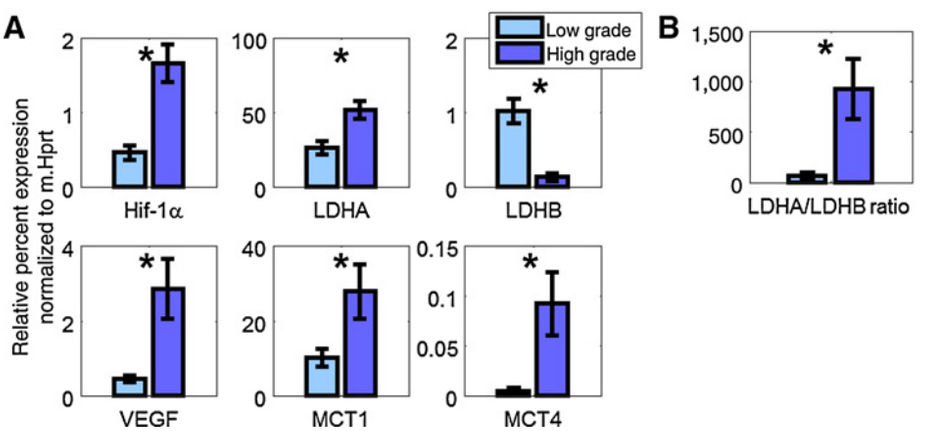

Figure 6.
A, mRNA expression level ± SE of *Hif1α* ($P < 0.01$), *Ldha* ($P < 0.01$), *Ldhb* ($P < 0.01$), *Vegf* ($P < 0.01$), *Mct1* ($P < 0.05$), and *Mct4* ($P < 0.01$) for the 9 low-grade and 10 high-grade TRAMP tumors studied; values given are relative percent expression normalized to m.Hprt. **B,** *Ldha*/*Ldhb* ratio ($P < 0.01$) for the same TRAMP tumors. *, significantly different.

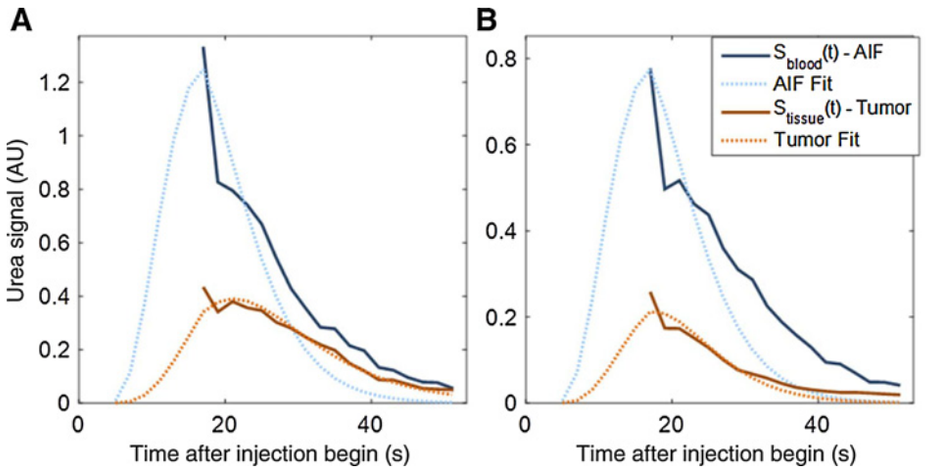

Figure 7.
Mean urea dynamic data (solid lines: blue, AIF; gold, tumor) for low-grade (**A**) and high-grade (**B**) TRAMP prostate tumors were fitted and k_{trans} and k_2 parameters calculated (high-grade $k_{trans} = 344$, $k_2 = 4{,}380$; low-grade $k_{trans} = 163$, $k_2 = 819$). The fit curves were extrapolated to the bolus arrival time at $t = 5$(s). In high-grade tumors, higher cellularity contributes to more rapid clearance of urea and low AUC (high-grade urea AUC = 1,407 ± 221; low-grade = 640 ± 94).

dynamics, increased LDH activity is a major factor contributing to the increase in the observed HP lactate signal in high-grade TRAMP tumors. The increased HP ^{13}C-lactate signal observed in high- versus low-grade prostate cancer was also associated with increased mRNA expression of lactate dehydrogenase-A (*Ldha*), decreased expression of *Ldhb*, as well as increased monocarboxylate transporters (*Mct1* and Mct*4*) that have a role in both pyruvate uptake and lactate export (5). LDHA and B are responsible for encoding the M and H subunits of LDH, and the high *Ldha*/*Ldhb* expression ratio observed in high-grade TRAMP tumors leads to the production of a predominance of the LDH5 isoenzyme (5M subunits) favoring increased lactate production. In patient studies, a high-serum LDH level is associated with aggressive disease and a poor survival for a variety of cancers (24, 25) including prostate cancer (26), and inhibition of the LDH-catalyzed production of lactate has become a therapeutic target (27, 28). Studies using patient biopsies and prostate tissue slices removed at surgery have demonstrated increased steady-state pools of lactate, HP ^{13}C-lactate production, increased LDH activity, and increased mRNA expression of *LDHA* and *MCT1* and *4* in prostate cancer tissues similar to what has been observed in the TRAMP model used in this study (29). Moreover, the k_{PL} fluxes observed in this preclinical study were in line with what was calculated from 2D dynamic HP ^{13}C MRSI studies in a phase 1 clinical trial of hyperpolarized [1-^{13}C]pyruvate in patients with prostate cancer (0.045 ± 0.025 s^{-1}; ref. 30). However, no correlation of k_{PL} with tumor grade was performed in these prior preclinical and clinical studies.

The 6-fold increase in *Mct4* observed in high-grade TRAMP tumors results in increased export of lactate out of the cells, which is important to sustaining a high glycolytic flux (31). Tumor excretion of lactic acid, combined with poor tumor perfusion, results in an acidic extracellular pH in tumors compared with normal tissue (16, 32), and this acidification of the tumor microenvironment has also been shown to occur in the TRAMP model (33). The resulting acidic environment promotes cancer aggressiveness and metastasis by facilitating a degradation of the extracellular matrix by proteinases (34, 35), increasing angiogenesis through the release of VEGF (36), and inhibiting the immune response to tumor antigens (37). Extracellular acidification also may render tumors chemo-resistant (37). Taken together, these observations suggest that not only increased lactic acid production, but also its efflux are important parameters associated with aggressive prostate cancer (38, 39). Moreover, tumor-specific metabolic shifts, such as increased production and efflux of lactate, can potentially be exploited for cancer therapy with minimal impact on normal tissues (32).

Hypoxia is a feature of many human cancers and has been implicated as an important biologically modulator of aggressiveness, clinical behavior, and treatment response in prostate cancer (40, 41). This study found a significant reduction in urea AUC in high- relative to low-grade TRAMP tumors, and an associated significant increase in hypoxia as measured by increased PIM staining. The oxygen-sensitive HIF1α transcription factor has been found to be upregulated in regions of tumor hypoxia and increases the expression of angiogenesis factors such as VEGF to increase oxygen delivery as well as increasing aerobic glycolysis through increasing expression and activity of key enzymes in the glycolytic pathway, including LDH (38). Consistent with this scenario, a significant increase was also observed in the mRNA expression of *Hif1α*, *Vegf*, and *Ldha*, as well as an increase in LDH activity in high- versus low-grade TRAMP tumors. Hypoxic prostate cancers, which induce HIF1α and glycolysis most strongly, tend to be of higher Gleason grade, are more invasive and metastatic, and less responsive to therapy than those with normal oxygen levels (41, 42).

Fitting the dynamic HP ^{13}C-urea to a Tofts-like 2–compartment model (20) demonstrated that k_{trans} was significantly increased in high- versus low-grade prostate cancer. The parameter k_{trans} represents the transfer of the contrast agent, hyperpolarized ^{13}C-urea, from the vasculature into the extravascular space and is therefore a function of both perfusion and permeability. Therefore, the observed increase in k_{trans} is presumably due to vascular hyperpermeability in high-grade TRAMP tumors, which is also consistent with increased expression of *Vegf* in high-grade tumors. The urea k_{trans} data are also consistent with prior gadolinium dynamic contrast-enhanced MRI studies of prostate cancer patients, in which high-grade prostate tumors demonstrated the earliest and greatest rate of enhancement and k_{trans} (43, 44). Although k_{trans} significantly increases, urea AUC significantly decreases in high-grade TRAMP prostate cancer tumors. The explanation for the decrease in urea AUC is the higher clearance of urea from high- versus low-grade tumors as observed in Fig. 7A and B. The increased rate of urea clearance (k_{ep}) was most likely due to a dramatic increase in the cellularity of high-grade TRAMP tumors

and a decrease in extravascular extracellular space (EES) and associated urea tissue distribution volume V_T ($V_T = k_{trans}/k_{ep}$). The measurement of k_{ep} was not directly possible in this study due to the fact that k_2 in our modeling was a lumped coefficient, that included urea clearance (k_{ep}) but was also heavily affected by urea T_1 relaxation and other signal loss mechanisms (Fig. 7; ref. 17).

Another important finding of this study was that there was significant heterogeneity (>2-fold) of k_{PL} and urea AUC in individual TRAMP tumors, with 90% of the high-grade TRAMP tumors demonstrating regions that had areas of the lowest urea AUC having the highest k_{PL}. Moreover, 50% of the high-grade TRAMP tumors demonstrated either lymph node or liver metastases, whereas none of the low-grade tumors demonstrated a urea AUC–k_{PL} mismatch nor any metastases. Although perfusion and metabolism are tightly coupled in most normal tissues, mismatches have been observed in a variety of tumors including lung, breast, liver, colon, and head and neck cancers, and this mismatch was associated with more aggressive disease (45, 46). A perfusion–metabolism mismatch, specifically, a high glycolytic rate relative to low perfusion, has been imaged in locally advanced breast cancer by ^{15}O-water and ^{18}F-FDG PET; this was associated with poor response to treatment and early relapse or disease progression (45, 46). This study demonstrated that the urea AUC–k_{PL} mismatch was similarly associated with aggressive prostate cancer in the TRAMP model. However, the relationship between urea AUC–k_{PL} mismatch and aggressive prostate cancer needs to be validated, and the relationship between urea AUC and more conventional measurement of perfusion or blood flow needs to be determined in future patient studies.

The TRAMP murine model used in this preclinical study, like all preclinical models, has its limitations. Most importantly, disease progression in this murine model is faster than what is observed in prostate cancer patients, with prostate cancer progressing from early-stage to late-stage disease in a matter of weeks instead of years. Although the pathologic progression of disease in this model mimics the human situation, it progresses from an admixture of normal glandular tissue and cancer to large areas of densely packed malignant cells in a much shorter period of time. Early- and late-stage disease is more homogenous in the TRAMP model than in the human situation due to a lower incidence of coexisting benign prostate tissue, early and late stage cancer. In addition, although there are significant lymph node metastases in the TRAMP model and some liver metastases, similar to the human situation, there are virtually no bone metastases, unlike the human situation. The data acquisition scheme and the compartmental modeling approach used in this study represented a trade-off between several factors. The dynamic data acquisition scheme utilized double spin-echo refocusing (47) in order to provide improved SNR for individual images, but at the expense of saturating signals at the edges of the RF coil, requiring the acquisition to start at the end, and causing loss of the earliest points of the dynamic data. With this acquisition approach, we found that a two-site unidirectional pyruvate-to-lactate model provided the most robust and reproducible fits. Our approach also did not use information from the AIF. There is potential to improve the kinetic modeling of metabolism and perfusion with acquisitions capturing the bolus input signal, incorporating the AIF, and by using advanced modeling methods such as those presented in Kazan and colleagues (48), Khegai and colleagues (49), and Bankson and colleagues (50).

In summary, the pathologic grade dependence of hyperpolarized pyruvate-to-lactate flux, urea k_{trans}, and AUC were measured in a single imaging acquisition after administration of hyperpolarized ^{13}C-pyruvate and ^{13}C-urea in a transgenic mouse model of prostate cancer. High HP ^{13}C-pyruvate to ^{13}C-lactate flux, low ^{13}C urea AUC, and high forward perfusion coefficient (k_{trans}) were found to be biomarkers of high-grade prostate cancer in this preclinical study. In addition, a substantial mismatch in urea AUC and a high pyruvate to lactate flux observed in this study were associated with highly proliferative disease with increased metastases. These hyperpolarized imaging biomarkers of aggressive prostate cancer, and their relationship to the perfusion–metabolism mismatch observed in prior studies, will clearly need to be better understood and validated in future patient studies. The likelihood of translating this hyperpolarized dual-agent MR approach is high because HP ^{13}C-pyruvate is already FDA IND-approved for ongoing clinical trials, and ^{13}C-urea has an excellent safety profile and is administered clinically at doses even higher than would be used for hyperpolarized MRI.

Disclosure of Potential Conflicts of Interest

D.B. Vigneron reports receiving commercial research grant from GE Healthcare. No potential conflicts of interest were disclosed by the other authors.

Authors' Contributions

Conception and design: H.-Y. Chen, P.E.Z. Larson, J. Kurhanewicz, D.B. Vigneron

Development of methodology: H.-Y. Chen, P.E.Z. Larson, R.A. Bok, C. von Morze, R. Delos Santos, N. Bahrami, M. Ferrone, J. Kurhanewicz, D.B. Vigneron

Acquisition of data (provided animals, acquired and managed patients, provided facilities, etc.): H.-Y. Chen, R.A. Bok, R. Sriram, R. Delos Santos, J. Delos Santos, M. Ferrone, J. Kurhanewicz, D.B. Vigneron

Analysis and interpretation of data (e.g., statistical analysis, biostatistics, computational analysis): H.-Y. Chen, P.E.Z. Larson, C. von Morze, R. Sriram, J. Delos Santos, J.W. Gordon, J. Kurhanewicz, D.B. Vigneron

Writing, review, and/or revision of the manuscript: H.-Y. Chen, P.E.Z. Larson, R.A. Bok, C. von Morze, R. Sriram, J.W. Gordon, M. Ferrone, J. Kurhanewicz, D.B. Vigneron

Administrative, technical, or material support (i.e., reporting or organizing data, constructing databases): R. Delos Santos, J. Delos Santos

Study supervision: R. Delos Santos, J. Kurhanewicz, D.B. Vigneron

Grant Support

This study was supported by grants from the Department of Defense (PC120148) and NIH (R01EB017449, R01EB013427, and P41EB013598, all to D.B. Vigneron; R01CA166655 to J. Kurhanewicz).

The costs of publication of this article were defrayed in part by the payment of page charges. This article must therefore be hereby marked advertisement in accordance with 18 U.S.C. Section 1734 solely to indicate this fact.

Received July 29, 2016; revised December 19, 2016; accepted April 13, 2017; published OnlineFirst April 20, 2017.

References

1. American Cancer Society.Cancer facts & figures: The American Cancer Society; 2015. Available from: http://www.cancer.org/research/cancerfacts statistics/cancerfactsfigures2015/.

2. Eggener SE, Mueller A, Berglund RK, Ayyathurai R, Soloway C, Soloway MS, et al. A multi-institutional evaluation of active surveillance for low risk prostate cancer. J Urol 2013;189:S19–25.

3. Chang ST, Westphalen AC, Jha P, Jung AJ, Carroll PR, Kurhanewicz J, et al. Endorectal MRI and MR spectroscopic imaging of prostate cancer: Developing selection criteria for MR-guided focal therapy. J Magn Reson Imaging 2014;39:519–25.
4. Muller BG, Futterer JJ, Gupta RT, Katz A, Kirkham A, Kurhanewicz J, et al. The role of magnetic resonance imaging (MRI) in focal therapy for prostate cancer: Recommendations from a consensus panel. BJU Int 2014;113:218–27.
5. Keshari KR, Sriram R, Van Criekinge M, Wilson DM, Wang ZJ, Vigneron DB, et al. Metabolic reprogramming and validation of hyperpolarized 13C lactate as a prostate cancer biomarker using a human prostate tissue slice culture bioreactor. Prostate 2013;73:1171–81.
6. Wilson DM, Kurhanewicz J. Hyperpolarized 13C MR for molecular imaging of prostate cancer. J Nucl Med 2014;55:1567–72.
7. Costello LC, Franklin RB, Zou J, Feng P, Bok R, Swanson MG, et al. Human prostate cancer ZIP1/zinc/citrate genetic/metabolic relationship in the TRAMP prostate cancer animal model. Cancer Biol Ther 2011;12:1078–84.
8. Gingrich JR, Barrios RJ, Foster BA, Greenberg NM. Pathologic progression of autochthonous prostate cancer in the TRAMP model. Prostate Cancer Prostatic Dis 1999;2:70–5.
9. Kurhanewicz J, Vigneron DB, Brindle K, Chekmenev EY, Comment A, Cunningham CH, et al. Analysis of cancer metabolism by imaging hyperpolarized nuclei: Prospects for translation to clinical research. Neoplasia 2011;13:81–97.
10. Beauregard JM, Williams SG, Degrado TR, Roselt P, Hicks RJ. Pilot comparison of F-fluorocholine and F-fluorodeoxyglucose PET/CT with conventional imaging in prostate cancer. J Med Imaging Radiat Oncol 2010;54:325–32.
11. Farsad M, Schiavina R, Franceschelli A, Sanguedolce F, Castellucci P, Bertaccini A, et al. Positron-emission tomography in imaging and staging prostate cancer. Cancer Biomark 2008;4:277–84.
12. Albers MJ, Bok R, Chen AP, Cunningham CH, Zierhut ML, Zhang VY, et al. Hyperpolarized 13C lactate, pyruvate, and alanine: Noninvasive biomarkers for prostate cancer detection and grading. Cancer Res 2008;68:8607–15.
13. Kim J-w, Gardner LB, Dang CV. Oncogenic alterations of metabolism and the Warburg effect. Drug Discov Today 2005;2:233–8.
14. Larson PE, Hu S, Lustig M, Kerr AB, Nelson SJ, Kurhanewicz J, et al. Fast dynamic 3D MR spectroscopic imaging with compressed sensing and multiband excitation pulses for hyperpolarized 13C studies. Magn Reson Med 2011;65:610–9.
15. Bahrami N, Swisher CL, Von Morze C, Vigneron DB, Larson PE. Kinetic and perfusion modeling of hyperpolarized (13)C pyruvate and urea in cancer with arbitrary RF flip angles. Quant Imaging Med Surg 2014; 4:24–32.
16. Wilson DM, Keshari KR, Larson PE, Chen AP, Hu S, Van Criekinge M, et al. Multi-compound polarization by DNP allows simultaneous assessment of multiple enzymatic activities in vivo. J Magn Reson 2010;205:141–7.
17. von Morze C, Larson PEZ, Hu S, Keshari K, Wilson DM, Ardenkjaer-Larsen JH, et al. Imaging of blood flow using hyperpolarized [13C]Urea in preclinical cancer models. J Magn Reson Imag 2011;33:692–7.
18. Hu S, Lustig M, Balakrishnan A, Larson PE, Bok R, Kurhanewicz J, et al. 3D compressed sensing for highly accelerated hyperpolarized (13)C MRSI with in vivo applications to transgenic mouse models of cancer. Magn Reson Med 2010;63:312–21.
19. Crane JC, Olson MP, Nelson SJ. SIVIC: Open-source, standards-based software for DICOM MR spectroscopy workflows. Int J Biomed Imaging 2013;2013:169526.
20. Tofts PS, Brix G, Buckley DL, Evelhoch JL, Henderson E, Knopp MV, et al. Estimating kinetic parameters from dynamic contrast-enhanced T(1)-weighted MRI of a diffusable tracer: Standardized quantities and symbols. J Magn Reson Imaging 1999;10:223–32.
21. Swisher CL, Larson PEZ, Kruttwig K, Kerr AB, Hu S, Bok RA, et al. Quantitative measurement of cancer metabolism using stimulated echo hyperpolarized carbon-13 MRS. Magn Reson Med 2014;71:1–11.
22. Feron O. Pyruvate into lactate and back: From the Warburg effect to symbiotic energy fuel exchange in cancer cells. Radiother Oncol 2009;92:329–33.
23. Hirschhaeuser F, Sattler UG, Mueller-Klieser W. Lactate: A metabolic key player in cancer. Cancer Res 2011;71:6921–5.
24. Petrelli F, Cabiddu M, Coinu A, Borgonovo K, Ghilardi M, Lonati V, et al. Prognostic role of lactate dehydrogenase in solid tumors: A systematic review and meta-analysis of 76 studies. Acta Oncol 2015;54:961–70.
25. Wulaningsih W, Holmberg L, Garmo H, Malmstrom H, Lambe M, Hammar N, et al. Serum lactate dehydrogenase and survival following cancer diagnosis. Br J Cancer 2015;113:1389–96.
26. Ryan CJ, Smith MR, Fizazi K, Saad F, Mulders PF, Sternberg CN, et al. Abiraterone acetate plus prednisone versus placebo plus prednisone in chemotherapy-naive men with metastatic castration-resistant prostate cancer (COU-AA-302): Final overall survival analysis of a randomised, double-blind, placebo-controlled phase 3 study. Lancet Oncol 2015;16: 152–60.
27. DeBerardinis RJ, Thompson CB. Cellular metabolism and disease: What do metabolic outliers teach us? Cell 2012;148:1132–44.
28. Kroemer G, Pouyssegur J. Tumor cell metabolism: Cancer's Achilles' heel. Cancer Cell 2008;13:472–82.
29. Tessem MB, Swanson MG, Keshari KR, Albers MJ, Joun D, Tabatabai ZL, et al. Evaluation of lactate and alanine as metabolic biomarkers of prostate cancer using H-1 HR-MAS spectroscopy of biopsy tissues. Magn Reson Med 2008;60:510–6.
30. Nelson SJ, Kurhanewicz J, Vigneron DB, Larson PEZ, Harzstark AL, Ferrone M, et al. Metabolic imaging of patients with prostate cancer using hyperpolarized [1-C-13]pyruvate. Sci Transl Med 2013;5:198ra108. doi: 10.1126/scitranslmed.3006070.
31. Dimmer KS, Friedrich B, Lang F, Deitmer JW, Broer S. The low-affinity monocarboxylate transporter MCT4 is adapted to the export of lactate in highly glycolytic cells. Biochem J 2000;350 Pt 1:219–27.
32. Parks SK, Chiche J, Pouyssegur J. Disrupting proton dynamics and energy metabolism for cancer therapy. Nat Rev Cancer 2013;13:611–23.
33. Korenchan D, Flavell R, Baligand C, Sriram R, Neumann K, Sukumar S, et al. Dynamic nuclear polarization of biocompatible 13 C-enriched carbonates for in vivo pH imaging. Chem Commun 2016;52:3030–3.
34. Estrella V, Chen T, Lloyd M, Wojtkowiak J, Cornnell HH, Ibrahim-Hashim A, et al. Acidity generated by the tumor microenvironment drives local invasion. Cancer Res 2013;73:1524–35.
35. Gatenby RA, Gawlinski ET, Gmitro AF, Kaylor B, Gillies RJ. Acid-mediated tumor invasion: A multidisciplinary study. Cancer Res 2006;66:5216–23.
36. Fukumura D, Xu L, Chen Y, Gohongi T, Seed B, Jain RK. Hypoxia and acidosis independently up-regulate vascular endothelial growth factor transcription in brain tumors in vivo. Cancer Res 2001;61:6020–4.
37. Lardner A. The effects of extracellular pH on immune function. J Leukoc Biol 2001;69:522–30.
38. Coller HA. Is cancer a metabolic disease? Am J Pathol 2014;184:4–17.
39. Dhup S, Dadhich RK, Porporato PE, Sonveaux P. Multiple biological activities of lactic acid in cancer: Influences on tumor growth, angiogenesis and metastasis. Curr Pharm Des 2012;18:1319–30.
40. Milosevic M, Warde P, Menard C, Chung P, Toi A, Ishkanian A, et al. Tumor hypoxia predicts biochemical failure following radiotherapy for clinically localized prostate cancer. Clin Cancer Res 2012;18:2108–14.
41. Wang L, Chen Z, Wang Q, Cao W, Jian Y, Wang S, et al. Expression of hypoxia-inducible factor 1 alpha and vascular endothelial growth factor in prostate cancer and its significance. Zhonghua Nan Ke Xue 2006;12:57–9.
42. Matsumoto S, Batra S, Saito K, Yasui H, Choudhuri R, Gadisetti C, et al. Antiangiogenic agent sunitinib transiently increases tumor oxygenation and suppresses cycling hypoxia. Cancer Res 2011;71:6350–9.
43. Oto A, Yang C, Kayhan A, Tretiakova M, Antic T, Schmid-Tannwald C, et al. Diffusion-weighted and dynamic contrast-enhanced mri of prostate cancer: Correlation of quantitative MR parameters with Gleason score and tumor angiogenesis. Am J Roentgenol 2011;197:1382–90.
44. Peng YH, Jiang YL, Yang C, Brown JB, Antic T, Sethi I, et al. Quantitative analysis of multiparametric prostate MR images: Differentiation between prostate cancer and normal tissue and correlation with Gleason score-A computer-aided diagnosis development study. Radiology 2013;267:787–96.
45. Mankoff DA, Dunnwald LK, Partridge SC, Specht JM. Blood Flow-metabolism mismatch: Good for the tumor, bad for the patient. Clin Cancer Res 2009;15:5294–6.
46. Mankoff DA, Dunnwald LK, Gralow JR, Ellis GK, Charlop A, Lawton TJ, et al. Blood flow and metabolism in locally advanced breast cancer: Relationship to response to therapy. J Nucl Med 2002;43:500–9.

47. Cunningham CH, Chen AP, Albers MJ, Kurhanewicz J, Hurd RE, Yen YF, et al. Double spin-echo sequence for rapid spectroscopic imaging of hyperpolarized 13C. J Magn Reson 2007;187:357–62.
48. Kazan SM, Reynolds S, Kennerley A, Wholey E, Bluff JE, Berwick J, et al. Kinetic modeling of hyperpolarized c-13 pyruvate metabolism in tumors using a measured arterial input function. Magn Resonance Med 2013; 70:943–53.
49. Khegai O, Schulte RF, Janich MA, Menzel MI, Farrell E, Otto AM, et al. Apparent rate constant mapping using hyperpolarized [1-C-13]pyruvate. NMR Biomed 2014;27:1256–65.
50. Bankson JA, Walker CM, Ramirez MS, Stefan W, Fuentes D, Merritt ME, et al. Kinetic modeling and constrained reconstruction of hyperpolarized [1-C-13]-Pyruvate offers improved metabolic imaging of tumors. Cancer Res 2015;75:4708–17.